RSC Advances

PAPER

View Article Online
View Journal | View Issue

Cite this: *RSC Adv.*, 2025, **15**, 36127

Sustainable hydrogen production *via* NH_3BH_3 hydrolysis using platinum nanoparticles decorated on solvent-free synthesized $LiNbWO_6$

Noemí Cristina Silva de Souza,[a] Beatriz Rodrigues Olímpio,[a] Gessica do Carmo Dias,[a] Juliana Peña Gomes,[b] Kleryton Luiz Alves de Oliveira,[a] Didier Astruc,[c] Tiago Almeida Silva,[a] Geraldo Magela de Lima*[b] and Renata Pereira Lopes Moreira*[a]

A novel catalyst for the controlled and safe evolution of hydrogen (H_2) fuel from ammonia borane (NH_3BH_3) is presented in this work based on platinum nanoparticles (PtNPs) decorated on $LiNbWO_6$ support. The $LiNbWO_6$ compound was successfully synthesized through an unprecedented solvent-free approach, *via* the solid-state method using calcination at 760 °C for 24 hours. This material was employed as a support for PtNPs in the hydrolysis reaction of ammonia borane for hydrogen generation. $LiNbWO_6$ and PtNPs/$LiNbWO_6$ were both characterized by various techniques. X-ray diffraction (XRD) confirmed that the crystalline structure of $LiNbWO_6$ was consistent with the JCPDS standard 84-1764. Fourier-transform infrared spectroscopy (FTIR) also corroborated the success of the novel solvent-free synthesis. Thermogravimetric analysis (TGA) indicated the high thermal stability of the support, with a mass loss of only approximately 1.5% up to 800 °C. Transmission electron microscopy (TEM) revealed the lamellar structure characteristic of the support, as well as the presence of finely dispersed Pt NPs with an average size of 2.80 nm. X-ray photoelectron spectroscopy (XPS) confirmed the presence of metallic platinum in the catalyst and demonstrated its robustness during reuse assays. The material proved to be an efficient support for platinum in the catalytic hydrolysis of ammonia borane, achieving a hydrogen generation rate (HGR) of 3974 mL H_2 $min^{-1} \cdot g^{-1}$, a value comparable to those reported in the literature.

Received 1st July 2025
Accepted 31st August 2025

DOI: 10.1039/d5ra04670j

rsc.li/rsc-advances

1. Introduction

In recent years, climate change resulting from the high consumption of fossil fuels, which release greenhouse gases, has intensified interest in hydrogen (H_2) gas as a sustainable energy alternative.[1] Although research on hydrogen-based technologies began in the 1970s, the storage and release of this gas remains costly and challenging, limiting its widespread use.[2]

Hydrogen gas is widely recognized as a clean fuel, as its use generates only water vapor as a byproduct. However, its production is still largely dependent on fossil fuels, such as coal reforming, a process that releases tons of CO_2 into the atmosphere.[3,4] Some common hydrogen production methods include steam methane reforming (SMR), where methane gas is mixed with steam reformer to produce synthesis gas (a mixture of CO and H_2). These reactions generally occur at high temperatures (700–800 °C).[5] Although SMR yields a high hydrogen output, the associated CO_2 emissions prevent the process from being fully sustainable.[6]

There are also thermochemical and biological processes (alternative routes) by which H_2 is produced from biomass. Biological conversion usually takes longer and requires maintaining a stable equilibrium state, whereas thermochemical conversion can produce products within a shorter time frame through heating. Thermochemical technologies include pyrolysis, gasification, combustion, and liquefaction, with gasification being the most widely applied method.[7]

In the water splitting process, water molecules are split into oxygen and H_2 when sufficient energy is provided. Water splitting can be performed by photolysis, thermolysis, or electrolysis.[8,9] Electrolysis is the most used technology, in which water is divided into H_2 and oxygen by an electric current flowing between two electrodes separated by an electrolyte.[10] However, due to the lack of adequate infrastructure for hydrogen storage and transport, large-scale production faces challenges in meeting current widespread demand.[8] Additionally, it has

[a]*Departament of Chemistry, Universidade Federal de Viçosa (UFV), Campus Universitário, Av. Peter Henry Rolfs, s/n, 36570-900 Viçosa-MG, Brazil. E-mail: renata.plopes@ufv.br*

[b]*Departament of Chemistry, Universidade Federal de Minas Gerais, Av. Antônio Carlos, 6627, Pampulha, Belo Horizonte, MG – CEP 31270-901, Brazil. E-mail: delima.geraldo@gmail.com*

[c]*Institut des Sciences Moleculaires, Université de Bordeaux, UMR CNRS 5255, Talence 33405 Cedex, France*

limitations due to its high electrical energy consumption and the need for optimized catalysts.[11]

In addition to the challenges associated with its production, the use of H_2 as a fuel faces significant obstacles related to storage and transportation due to its low density, low boiling point, and high flammability. Storing H_2 in its gaseous form requires compression between 100 and 400 bar, whereas in its liquid form, it demands cryogenic conditions around −253 °C to enable viable storage and transport.[12]

Chemical storage appears to be a promising alternative to circumvent the high flammability and potential for explosions of H_2. Liquid compounds, such as organic carriers, hydrazine, alcohols, and formic acid, or solid materials, including metal hydrides, borohydrides, amides, imides, and ammonium borane, are under investigation. In both cases, H_2 gas is released through thermal or catalytic decomposition.[13]

Complex hydrides are characterized by the presence of an anionic complex, where H_2 is covalently bonded to a metal or a non-metal, as seen in $[BH_4]^-$, $[AlH_4]^-$, $[NH_2]^-$, $[AlH_6]^{3-}$, and $[NiH_4]^{4-}$. These anions interact electrostatically with one or more cations, formed by alkali metals, alkaline earth metals, transition metals, or rare earth elements groups.[14]

Ammonium borane (AB), NH_3BH_3, is a complex hydride, a class of compounds that has garnered significant interest in recent years.[15] In the NH_3BH_3 molecule, the hydrogen atoms bonded to boron and nitrogen carry partial negative and positive charges, respectively, acting as hydridic ($H^{\delta-}$) and protonic ($H^{\delta+}$) hydrogen atoms. The attractive interactions between these hydrogen atoms in adjacent molecules lead to the formation of $N^{\delta-}$–$H^{\delta+}$…$H^{\delta-}$–$B^{\delta+}$ bonding, which stabilizes the crystal structure.[16] The presence of these bonds imparts high solid-state stability and remarkable resistance to air humidity, distinguishing it from most inorganic hydrides.[16]

H_2 production from AB is a promising strategy due to its low molecular weight (30.7 g mol^{-1}) and high H_2 storage capacity (19.6% wt).[13,15] Additionally, AB hydrolysis stands out as a safe and stable process for H_2 generation.[15,17] The hydrolysis of AB can occur in the presence of a catalyst under ambient conditions, *i.e.*, at room temperature and atmospheric pressure, as shown in eqn (1). For every mole of AB, 3 moles of H_2 gas are released.[3]

$$NH_3BH_3\ (aq) + 4H_2O\ (l) \rightarrow NH_4B(OH)_4\ (aq) + 3H_2\ (g) \quad (1)$$

The only by-product of the reaction is metaborate, whose regeneration can be effectively achieved through mechanochemical methods using ball milling with MgH_2. Ball milling provides the mechanical energy necessary to break and reform chemical bonds, while MgH_2 acts as a reducing agent, facilitating the regeneration of the hydrogen-atom-rich compound.[18]

The catalytic hydrolysis of AB requires the use of metal NP[15] such as Co and Ru,[19] Rh and Co[20] and Pt.[21–23] However, the high surface energy of NPs tends to favor their self-aggregation, resulting in a decrease in their catalytic activity.[24] To mitigate this effect, various support materials have been investigated,[15] such as carbon-based structures,[25] polymers[21] and metal–organic frameworks.[26]

Niobium compounds have been extensively utilized in a wide range of applications, with a notable emphasis on heterogeneous catalysis.[24,27] Among these, stand the $ABXO_6$ family (where A = alkali ion; B = Nb; X = W or Mo) due to its ferroelectric properties and its typical high ionic conductivity and dielectric permittivity at elevated temperatures.[28] One prominent example, $LiNbWO_6$, features a layered structure in which cations and anions are arranged into distinct layers and plates, respectively.[29] This material is distinguished by its high thermal and chemical stability, large surface area, ion-exchange capacity, and tunable interlayer spacing. These compounds can crystallize in various structures, including cubic (space group $Fd\bar{3}m$), orthorhombic (*Pnma* or $Pca2_1$), and tetragonal (space group $P\text{-}421m$).[30] These structural phases are interconvertible and depend on temperature and pressure. To the best of our knowledge, the present study represents the first report of $LiNbWO_6$ synthesized *via* a solvent-free method being employed as a support in this catalytic system, underscoring both the originality and the potential impact of this strategy. Investigating such material offers a promising opportunity to harness and tailor its unique properties for catalytic purposes.

Given the above, the aim of this work is the synthesis of lithium niobate tungstate ($LiNbWO_6$) *via* a solid-state method, using a sustainable, solvent-free process, and employing it as support for Pt NPs, aiming at the control release of H_2 from AB hydrolysis.

2. Experimental

2.1. Reagents

The reagents used in this work are of analytical grade. Sodium borohydride 98% (CAS 16940-66-2) was obtained from Neon. Sodium hydroxide in microbeads 97% (CAS 1310-73-2) was obtained from Cromoline. Hexachloroplatinic acid (37–50% Pt) (CAS 18497-13-7), ammonium borane complex 95% (CAS 13774-81-7), and deuterium oxide 99% (CAS 7789-20-0) were purchased from Sigma-Aldrich. Lithium carbonate (CAS 554-13-2) and tungsten trioxide (CAS 1314-35-8) (81–83%) were purchased from Synth, while niobium pentoxide pentahydrate (CAS 1313-96-8) and nitric acid P.A. (64–66%) (CAS 7697-37-2) were obtained from A.C.S.

All solutions used in this work were prepared using ultrapure water, obtained through the Milli-Q system (Millipore Corporation), and were prepared immediately before use.

2.2. Synthesis of $LiNbWO_6$

The $LiNbWO_6$ compound was synthesized by the solid-state method, following a procedure adapted from Wu *et al.* (2022).[31] Stoichiometric amounts of WO_3, Li_2CO_3, and $Nb_2O_5 \cdot 5H_2O$ (in a 2 : 1 : 1 ratio) were mixed in a mortar, and the resulting mixture was compacted into pellets. The pellets were then placed in an alumina crucible and heated at 760 °C for 12 hours in a Lindberg/Blue M tubular furnace (6.0 kW–220 V). After heating, the furnace cooled to room temperature. The obtained pellets were then ground and mixed in a mortar and reformed. The heating and cooling process was repeated, and

finally, the resulting $LiNbWO_6$ was ground again and stored at room temperature.

2.3. Synthesis of platinum nanoparticles decorated on $LiNbWO_6$ (PtNPs/$LiNbWO_6$)

The catalyst was synthesized by dispersing 20 mg of $LiNbWO_6$ in 5 mL of ultrapure water under magnetic stirring for 10 minutes to ensure a uniform dispersion. Then, a specific volume of a platinum stock solution was added, maintaining 3 mmol% of Pt relative to the AB, and stirring was continued for an additional 10 minutes. Subsequently, 1.00 mL of a $NaBH_4$ solution (1.00 mol L^{-1}) was introduced into the system. After the reduction reaction, the material was centrifuged at 4000 rpm for 7 minutes. The obtained solid was washed with ultrapure water and centrifuged under the same conditions three times to ensure complete removal of excess $NaBH_4$. The synthesized catalyst was then used in the hydrolysis reaction of NH_3BH_3 for hydrogen gas production.

2.4. Characterization

X-ray diffraction (XRD) analysis was performed using a Bruker D8-Discover diffractometer with Cu-Kα radiation (λ = 0.1541 nm), with a 2θ angular range of 10° to 50°.

Transmission Electron Microscopy (TEM) was conducted using a Tecnai G2-20 SuperTwin FEI-200 kV microscope, equipped with a Si–Li detector (EDAX) for Energy Dispersive X-ray Spectroscopy (EDS) analysis.

Raman spectroscopy was performed using a micro-Raman spectrometer (Renishaw 16 InVia) with a Nd-YAG laser (λ_0 = 633 nm) and a 50× objective lens (Olympus B × 17 41). The sample data acquisition time was set to 10 s.

Fourier-transform infrared (FTIR) spectroscopy was carried out using a BRUKER ALPHA II spectrophotometer (USA) equipped with an attenuated total reflectance (ATR) accessory in the 400–4000 cm^{-1} range, with 16 scans and 4 cm^{-1} spectral resolution.

Thermal characterization was performed using a Shimadzu DTG60H thermobalance under an inert nitrogen atmosphere with a flow rate of 50 mL min^{-1}, over a temperature range of 30 to 800 °C. Simultaneous Thermogravimetric (TG) and Differential Thermal Analysis (DTA) data were collected. During the heating cycle, the temperature was increased at a rate of 10 °C min^{-1}. TG curves were differentiated to the first order (DTG) to confirm thermal phenomena.

The nitrogen adsorption and desorption isotherm of $LiNbWO_6$ was determined using the Nova 600 Series equipment from Anton Paar. The samples were subjected to the degassing process at 120 °C for 4 hours. The Brunauer–Emmett–Teller (BET) method was used to calculate the surface area.

The zeta potential of materials at different pH values was determined using the Malvern Zetasizer Nano ZS90 (Malvern, UK) equipment. $LiNbWO_6$ and PtNPs/$LiNbWO_6$ samples at 40 mg L^{-1} were prepared in 0.1 mol L^{-1} sodium chloride solution and the pH was adjusted to different values (2, 4, 6, 8, 10 and 12) using HCl or NaOH solutions, both at 0.1 mol L^{-1}.

The catalyst's chemical composition and oxidation states were analyzed using X-ray photoelectron spectroscopy (XPS). Measurements were carried out with a Thermo Scientific K-alpha system, equipped with a monochromatic Al anode source operating at a Kα energy of 1486 eV.

The diffuse reflectance was measured using a Thermo Scientific Evolution Array UV-vis spectrophotometer (Thermo Fisher Scientific).

2.5. Hydrogen evolution from NH_3BH_3

A 20 mg mass of the freshly prepared Pt NPs/$LiNbWO_6$ material, containing 3 mmol% of Pt relative to AB, was dispersed in 2.00 mL of Milli-Q water and placed in a Schlenk tube. The tube was connected to a water-filled burette, allowing the produced gas to displace the water column, whose displacement was measured during the reaction (Fig. S1). After assembling the system, 1.00 mL of NH_3BH_3 solution (0.580 mmol L^{-1}) was injected through the septum using a syringe. During the experiments, the system was kept under constant stirring at a controlled temperature of 27 °C (300.15 K) and atmospheric pressure (0.93 atm).

The rate constant was determined according to eqn (2).

$$k = \frac{3\mathrm{d}[NH_3BH_3]}{\mathrm{d}t} = \frac{\mathrm{d}[H_2]}{\mathrm{d}t} \quad (2)$$

The activation energy was determined according to eqn (3).

$$\ln(k) = \ln(A)\frac{E_a}{RT} \quad (3)$$

where k is the reaction rate constant, A is the pre-exponential factor, E_a is the activation energy in kJ mol^{-1}, R is the universal gas constant, and T is the temperature in Kelvin.

The Hydrogen Generation Rate (HGR) was calculated according to eqn (4).

$$HGR = \frac{\Delta V(H_2)}{\Delta t \times m_{cat}} \quad (4)$$

where $\Delta V(H_2)$ is the change in hydrogen volume in mL, Δt is the time variation in minutes, and m_{cat} is the catalyst mass in grams.

Several parameters influencing the reaction were evaluated: (1) PtNPs dosage; (2) $LiNbWO_6$ support dosage; (3) NH_3BH_3 concentration; (4) temperature; (5) presence of NaOH; (6) material durability; and (7) kinetic isotope effect.

2.5.1 PtNPs dosage. The influence of PtNP dosage was investigated using doses of 0.20, 0.50, 1.00, 3.00, and 5.00 mmol% relative to NH_3BH_3. During these experiments, other parameters were kept constant: 10 mg of $LiNbWO_6$, 1.00 mL of NH_3BH_3 solution (0.580 mmol L^{-1}), and a temperature of 300.15 K.

2.5.2 Evaluation of $LiNbWO_6$ support dosage. Different $LiNbWO_6$ support masses were evaluated: 0, 10, 15, 20, and 30 mg. The fixed conditions included 3.00 mmol% of PtNPs, 1.00 mL of NH_3BH_3 solution (0.580 mmol L^{-1}), and a temperature of 300.15 K.

2.5.3 Evaluation of NH_3BH_3 concentration. NH_3BH_3 concentrations of 0.40, 0.50, 0.58, and 0.70 mmol L^{-1} were evaluated. During the experiments, the fixed parameters were:

20 mg of $LiNbWO_6$, 3.00 mmol% of platinum, and a temperature of 300.15 K.

2.5.4 Evaluation of temperature. The influence of temperature was evaluated at 293.15, 300.15, 313.15, and 323.15 K, while keeping the following parameters constant: 20 mg of $LiNbWO_6$, 3.00 mmol% of PtNPs, and 1.00 mL of NH_3BH_3 solution (0.580 mmol L^{-1}).

2.5.5 Evaluation of NaOH concentrations. NaOH concentrations of 0.010, 0.025, 0.050, and 0.075 mol L^{-1} were evaluated, while other parameters remained constant: 20 mg of $LiNbWO_6$, 3.00 mmol% of PtNPs, 1.00 mL of NH_3BH_3 solution (0.580 mmol L^{-1}), and a temperature of 300.15 K.

2.5.6 Evaluation of material durability. After each catalyst use cycle, the Schlenk tube was detached to reset the burette before starting a new cycle. In each repetition, 1.00 mL of fresh NH_3BH_3 solution (0.580 mmol L^{-1}) was injected without washing the catalyst. The fixed parameters were 20 mg of $LiNbWO_6$, 3.00 mmol% of PtNPs, and a temperature of 300.15 K. Durability was assessed over 10 consecutive cycles, which were carried out under the same conditions.

2.5.7 Evaluation of kinetic isotope effect (KIE). To investigate the catalytic reaction mechanism, 20 mg of freshly prepared $PtNPs/LiNbWO_6$, washed with isopropyl alcohol and vacuum-dried, was added to a Schlenk tube containing 2.00 mL of deuterium oxide (D_2O). The tube was sealed with a septum and connected to a water-filled burette. Then, 1.00 mL of NH_3BH_3 solution (0.580 mmol L^{-1}) in deuterium oxide (D_2O) was introduced into the system. All reactions were conducted at 300.15 K. KIE was calculated according to eqn (5).

$$\mathrm{KIE} = \frac{\mathrm{KH}}{\mathrm{KD}} \tag{5}$$

2.5.8 Experiments were conducted under four conditions. (i) Absence of light, (ii) ambient natural light provided by a tubular LED lamp (T8, 10 W, 6500 K), (iii) a UV chamber (LUCMAT LAMPS, germicidal fluorescent lamp, 15 W GL, λ = 100–280 nm), and (iv) in the presence of the hole scavenger sodium oxalate at a concentration of 52.6 mmol L^{-1}.

3. Results and discussion

3.1. Material characterization

The material was analyzed by X-ray diffraction, and the results are shown in Fig. 1(a).

The solvent-free synthesis of $LiNbWO_6$ was successful, as evidenced by its tetragonal structure with space group *P*-421*m*, which matches the reference pattern JCPDS 84-1764.[32] The corresponding crystal structure (lattice structure) is shown in Fig. S2. The diffraction patterns of $LiNbWO_6$ remained unaffected after the incorporation of PtNPs, indicating the preservation of its crystalline structure without significant modifications. The absence of detectable Pt signals is likely attributed to their low loading and high dispersion within the matrix.

The solid-state method offers several advantages over hydrothermal/solvothermal, sol–gel, coprecipitation, and other wet-chemical methods. Firstly, it is a relatively simple and scalable process that does not require complex solvents, surfactants, or high-pressure vessels, which reduces costs and technical complexity. Secondly, the solid-state reaction promotes high crystallinity and phase purity due to the high temperatures applied during synthesis. Additionally, this method allows better control of stoichiometry by using precise amounts of starting materials and avoids contamination that can arise from solvent residues. Finally, the solid-state approach is well-suited for producing bulk quantities of materials like $LiNbWO_6$, making it advantageous for practical applications and further processing.

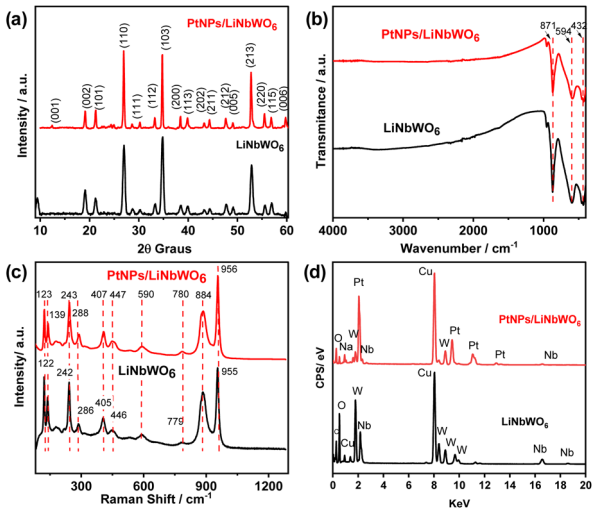

Fig. 1 (a) X-ray diffraction pattern, (b) FT-IR spectra, (c) Raman spectra and (d) EDS spectra of LiNbWO6 and $PtNPs/LiNbWO_6$.

Thermogravimetric analysis (TGA) of $LiNbWO_6$ was performed (Fig. S3), revealing that the material remained stable up to 800 °C, with a total mass loss of approximately 1.5%. The tetragonal *P*-421*m* structure is known for its thermal stability and does not typically decompose at temperatures below 800 °C. The observed mass loss may be attributed to the release of residual adsorbed, structurally bound, or strongly bound water remaining in the material after synthesis.[33]

The $LiNbWO_6$ before and after PtNPs decorating were characterized by FTIR (Fig. 1(b)). The characteristic bands of $LiNbWO_6$ at 871 and 594 cm^{-1} were attributed to the stretching vibrations of the Nb=O and O–W–O bonds, respectively.[29] These frequencies indicate that the lithium niobate tungstate showed no significant differences in the overall position of the bands after the deposition of PtNPs, despite small shifts in the band positions. These shifts may suggest subtle interactions between the Pt nanoparticles and the $LiNbWO_6$ structure, without causing significant alterations in the material's overall structure. W. Chen *et al.* (2018)[34] observed that the FTIR spectrum of platinum nanoparticles supported on carbon nanotubes (CNT) does not display the Pt–O vibrations, as a consequence of the overlap of these peaks with those of the CNT support. Similarly, Asim *et al.* (2020)[35] reported, based on FTIR analysis, that the structure of Ni_2P remained unchanged after the deposition of platinum.

Raman spectra of $LiNbWO_6$ and PtNPs/$LiNbWO_6$ are displayed in Fig. 1(c), display similar bands. The bands between 400 and 100 cm^{-1} can be attributed to the bending vibration of WO. The bands between 800 and 400 cm^{-1} are associated with ν(WO) vibrations. The ν(W═O) stretching band is located at 955 cm^{-1}, and the ν(Nb═O) band is at 884 cm^{-1}. These results are also consistent with those found by Fayad *et al.*, (2020),[36] who simultaneously monitored acidity and intercalation for transition metal oxides into liquid media. Additionally, Bekkali & Clet, (2025)[37] used Raman spectroscopy for the discrimination of materials in molybdate and tungstate layers operating at the solid–liquid interface.

The surface charge and stability of the nanoparticles in suspension were determined by Zeta potential (ζ), as shown in Fig. S4, where $LiNbWO_6$ exhibited a negative surface charge that became more negative with an increase of pH, enhancing its suspension stability, with ζ at pH 6 being -22.45 ± 2.76 mV. A similar behavior was observed for PtNPs/$LiNbWO_6$. Zeta potential values higher than +30 mV or lower than −30 mV tend to favor particle dispersion, while values close to zero promote aggregation.[38] Cordero-Edwards *et al.* (2016)[39] noted that, in water adsorption studies on $LiNbO_3$, a material structurally similar to $LiNbWO_6$, the adsorption of hydroxyl groups (OH^-) is favored under certain polarization conditions, contributing to the development of a negative surface charge.

Nitrogen physisorption analysis of $LiNbWO_6$ was performed, and the results are presented in Fig. S5. The material exhibited a type II isotherm, which is characteristic of macroporous or non-porous solids.[40] The specific surface area of $LiNbWO_6$ was determined to be 1.013 $m^2\ g^{-1}$, increasing to 2.730 $m^2\ g^{-1}$ for PtNPs/$LiNbWO_6$, as determined by the BET model. Similar materials with structures related to $LiNbWO_6$ have also shown relatively low surface areas. For instance, β-$BiNbO_4$ presented a surface area of 7.26 $m^2\ g^{-1}$ when calcined at 700 °C,[41] while $LiNbO_3$ and $LiNb_3O_8$ exhibited surface areas of 3.91 $m^2\ g^{-1}$ and 0.96 $m^2\ g^{-1}$, respectively.[42]

$LiNbWO_6$ was characterized by TEM, and the results are shown in Fig. 2. The material exhibited a layered structure (Fig. 2(a)). The interplanar distance of 0.33 nm (Fig. 2(b)), is consistent with the value reported by Cheng *et al.*[28]

The images show that the spherical PtNPs are uniformly dispersed over the support (Fig. 2(c)). Fig. 2(d) shows that the Pt nanoparticles have an average size of 2.80 ± 0.58 nm, as also highlighted in the insert of Fig. 2(d). A similar particle size (2.8 nm) was reported by Uzundurukan & Devrim, (2019)[43] in their work using platinum-supported carbon nanotube-graphene hybrids for the hydrolysis of ammonium borane.

The XPS spectra of PtNPs/$LiNbWO_6$ are presented in Fig. 3. The W 4f peaks centered at 35.8 and 37.8 eV (Fig. 3(c)) correspond to the W $4f_{7/2}$ and W $4f_{5/2}$ orbitals of tungsten in the +6 oxidation state (W^{6+}).[44] High-resolution analysis of the Pt 4f region (Fig. 3(d)) shows two sets of doublets. The more intense doublet, with binding energies at 71.3 eV (Pt $4f_{7/2}$) and 74.5 eV (Pt $4f_{5/2}$), is characteristic of metallic platinum (Pt^0).[45] The two Nb3d peaks observed at approximately 207.5 and 210.2 eV (Fig. 3(e)) correspond to Nb $3d_{5/2}$ and Nb $3d_{3/2}$, respectively, confirming that niobium is present in the +5 oxidation state

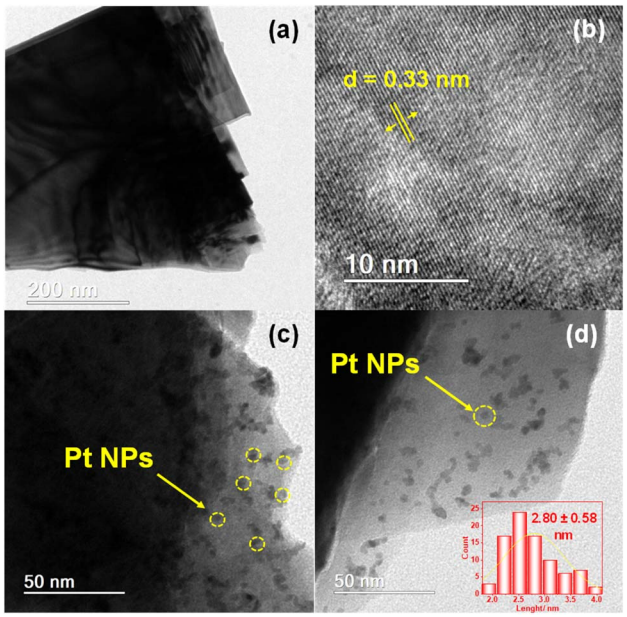

Fig. 2 Transmission electron microscopy (TEM) images of $LiNbWO_6$ (a) and (b); PtNPs/$LiNbWO_6$ (c) and (d) with insert showing the PtNPs size distribution.

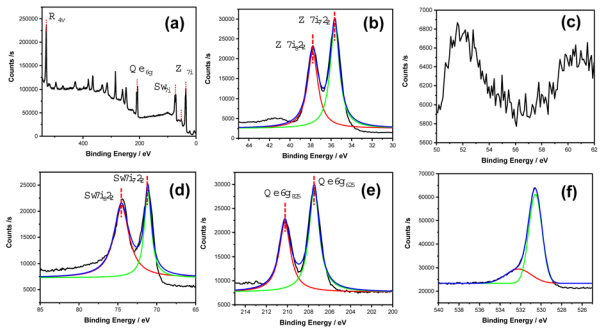

Fig. 3 XPS (a) survey spectra of PtNPs/$LiNbWO_6$, (b) W4f, (c) Li1s, (d) Pt4f, (e) Nb3d, (f) O1s signals.

(Nb^{5+}).[44] Fig. 3(f) shows the O 1s spectrum with binding energies at around 530.6 and 532.3 eV, which are attributed to lattice oxygen and adsorbed oxygen species, respectively.[44] These robust characterizations confirm the identity of PtNPs/$LiNbWO_6$, qualifying the following tests for the catalytic hydrogen production from the decomposition of ammonium borane.

3.2. Hydrogen evolution from NH_3BH_3

The effect of the catalyst dose was initially evaluated (Fig. S6(a)). A plot showing the data as a function of volume is presented in Fig. S7. The increase of Pt NPs dose from 0.2 to 3 mmol% enhanced the system's kinetics and raised the HGR from 1008 to 3458 mL H_2 min^{-1} g^{-1}. However, at 5 mmol%, no further improvement in the hydrogen generation rate was observed. This could be due to an excess of catalyst, which, due to its tendency to agglomerate, may have interfered with the

substrate's interaction with the active sites. Asim *et al.*, (2023)[35] employed platinum in combination with a metal phosphide (Ni_2P) to develop the Pt@Ni_2P catalyst, which was subsequently applied in the hydrolysis of ammonium borane. In their evaluation of catalyst dosage, the authors observed that the induction period was longer at lower catalyst concentrations and decreased with increasing catalyst amounts, attributed to the greater number of available active sites. The reaction order determined by Asim *et al.* (2023)[35] was 1.20, which is consistent with the value obtained in this study (1.16), as shown in Fig. S6(b).

The hydrogen production from NH_3BH_3 was assessed using varying amounts of support, with the lowest efficiency observed in the absence of any support (Fig. 4(a)). Metal nanoparticles are inherently unstable and tend to aggregate into larger particles, which limits their reusability and catalytic activity. An effective strategy to mitigate this instability is the immobilization of Pt NPs on supports with a high surface area.[46]

To evaluate the effect of $LiNbWO_6$ on the catalyst, experiments were conducted with different amounts of material. It was observed that increasing the amount of support enhanced reaction efficiency, resulting in a HGR of 3974 mL H_2 min^{-1} g^{-1} (Fig. 4(b)). However, no further kinetic enhancement occurred with amounts exceeding 20 mg. Therefore, 20 mg of $LiNbWO_6$ was selected for subsequent experiments. During hydrolysis in the presence of the support, without Pt NPs, only a negligible volume of gas was produced. This confirmed that the platinum active sites on the catalyst surface play a crucial role in promoting hydrogen generation from NH_3BH_3.

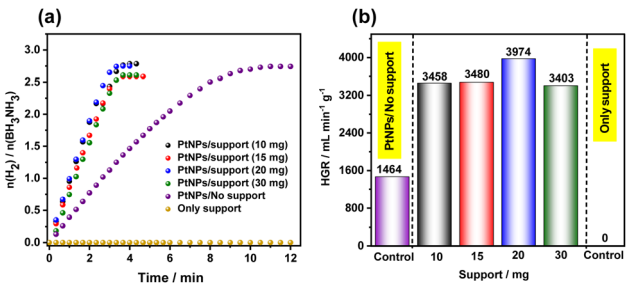

Fig. 4 (a) Evaluation of the influence of $LiNbWO_6$ support on hydrogen evolution from NH_3BH_3 (b) HGR for different amounts of support. Conditions: 0.58 mmol of ammonium borane, 3 mmol% of Pt NPs, temperature: 27 °C.

Fig. S8(a) shows the effect of AB concentration on the hydrolysis reaction. The results indicate that the reaction rate was not significantly affected by the AB concentration, suggesting a reaction order close to zero with respect to AB. This is further supported by the linear fit of ln(HGR) *versus* ln[AB], which yielded a slope of −0.37, as shown in Fig. S8(b). A similar behavior was reported by Guan *et al.*, (2024),[47] who employed a RuPt–Ti catalyst to investigate hydrogen atom activation pathways during AB hydrolysis.

The addition of NaOH is known to enhance the electronic properties of the catalyst and strengthen its interaction with NH_3BH_3, as reported by Wang *et al.* (2017).[48] Above a certain concentration, NaOH present a negative effect on the reaction rate, because its excess nanocatalyst coverage prevents the substrate adsorption and activation.[15,49,50] Indeed, as shown in Fig. S9, increasing the NaOH concentration from 0 to 0.01 mmol led to a progressive decrease in the hydrogen generation rate (HGR), with the effect becoming more pronounced at higher concentrations, as shown in Fig. S9(a) and (b). This reduction in HGR may be attributed to the excessive presence of hydroxyl ions, which can inhibit the reaction, a phenomenon also observed by Sait Izgi *et al.* (2019),[51] who noted that hydroxyl concentrations above an optimal level negatively affect HGR.

The rate law was proposed after evaluating the catalyst dosage and NH_3BH_3 concentration, as shown in eqn (6). NaOH was excluded because it influences the reaction rate negatively.

$$r = k \times [\text{catalyst}]^{1.16} \times [NH_3BH_3]^{-0.37} \quad (6)$$

The hydrolysis reaction was carried out at different temperatures (from 293.15 to 323.15 K), and the results are shown in Fig. S10. It is observed that the increase in the hydrogen generation is proportional to temperature. Using the rate constant data, the Arrhenius plot was constructed (Fig. S10, insert). A linear regression model was fitted to the experimental data, yielding a correlation coefficient (R^2) of 0.9583. The

Table 1 Performance of different catalysts in hydrogen evolution from ammonia borane

Catalyst	Temperature (°C)	[a]aE_a	[b]bHGR	Ref.
PtNi@SiO_2	30	54.76	1475	53
Cobalt-tungsten-boron-phosphorus porous particles supported on Ni foam (Co–W–B–P/Ni)	30	29.0	4000	56
Polyacrylonitrile polymeric (PAN/CoAc) and metal oxide (Co_3O_4/Nfs) nanofibrous structured composite	60	—	2540	57
Nanostructured Co–Mo–B thin film (Co–Mo–B)	25	41.7	5100	58
NiCo nanorod array supported on copper foam	25	19.2	1030	59
P-induced Co-based interfacial phosphides (Co-CoP-NC/NF)	25	30.6	2500	60
Pt–Ni–Co trimetallic nanoparticles anchored on graphene oxide	35	43.22	540	52
Nickel–iron–phosphide catalysts supported on Ni foam (Ni–Fe–P/Ni foam)	30	42.0	700	61
$Ni_{0.25}Co_{0.75}O$ nanowire array supported on Cu@CuO foam	25	—	4348	62
PtNPs/$LiNbWO_6$	**27**	**38.74**	**3974**	**This work**

[a] kJ mol^{-1}. [b] mL H_2 $min^{-1}\cdot g^{-1}$.

activation energy of 38.74 kJ mol^{-1}, determined in this work, is lower compared to some results in the literature (Table 1). Mansur Ahmed *et al.* (2024)[52] reported an activation energy of 43.22 kJ mol^{-1} using $Pt_{0.8}Ni_{0.1}Co_{0.1}$@GO. Qi *et al.* (2016)[53] obtained 54.76 kJ mol^{-1} with Pt@Ni core–shell nanoparticles. These values confirm the high efficiency of the catalyst used in this work.

Studies indicate that, in the mechanism of hydrogen gas release, one hydrogen atom originates from ammonium borane (AB) and the other from a water molecule. An effective approach to identifying the rate-determining step (RDS) of the reaction is the analysis of the kinetic isotope effect (KIE), as shown in eqn (5). The KIE was evaluated for the Pt NPs/$LiNbWO_6$ system, and the results are presented in Fig. 5. A KIE value of 6.76 was observed. KIE values in the range of 2 to 7 typically indicate that the RDS involves the formation or cleavage of a bond with the isotopically labeled atom. On the other hand, values between 0.7 and 1.5 suggest that no bond involving the substituted atom is formed or broken during this step.[54] These findings indicate that the step involving the water molecule is the rate-determining step in the hydrogen release process.

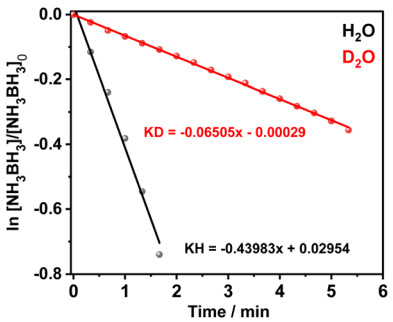

Fig. 5 Evaluation of the Kinetic Isotope Effect (KIE) in H_2O and D_2O during the hydrogen evolution reaction from NH_3BH_3. Conditions: support (20 mg); PtNPs/$LiNbWO_6$ catalyst (3.00 mmol%); NH_3BH_3 (0.500 mol L^{-1}).

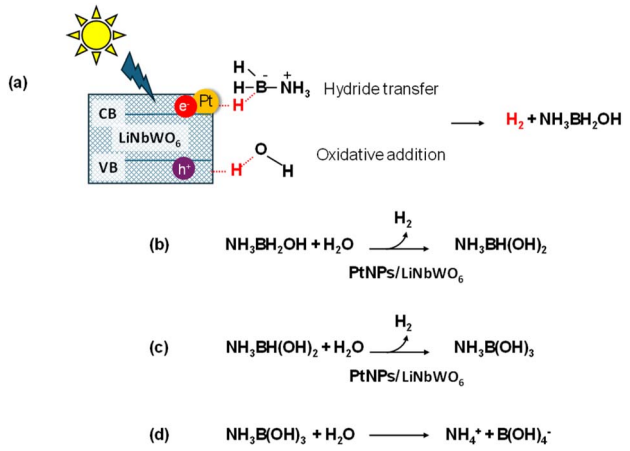

Fig. 6 (a) Schematic illustration of photocatalysis in the PtNPs/$LiNbWO_6$ system for ammonia borane hydrolysis, involving hydride transfer and oxidative addition, leading to the generation of H_2 and NH_3BH_2OH. (b) First hydrolysis step: NH_3BH_2OH reacts with H_2O, releasing H_2 and forming $NH_3BH(OH)_2$ in the presence of PtNPs/$LiNbWO_6$. (c) Second hydrolysis step: $NH_3BH(OH)_2$ reacts with H_2O, releasing H_2 and forming $NH_3B(OH)_3$. (d) Final step: $NH_3B(OH)_3$ in aqueous medium yields NH_4^+ and $B(OH)_4^-$.

In this context, the large KIE value implies that the step involving the activation or cleavage of the O–H bond in the water molecule is rate-limiting, rather than any step related to AB. Thus, initial oxidative addition of B–H bond of AB on the Pt surface rapidly forms a Pt-hydride in which this electron-rich hydridic atom becomes hydrogen-bonded to a positively charged hydrogen atom of water, weakening the involved water O–H bond that is then cleaved by Pt in the rate-determining step.[50,55] Based on these findings, a reaction pathway is proposed (Fig. 6).

Experiments under light exposure were performed. The hydrogen generation rate (HGR) followed the increasing order: dark ≈ in the presence of the hole scavenger < UV light < natural light, highlighting the significant role of light exposure in the process efficiency, as shown in Fig. S11. The mechanism of hydrogen evolution from NH_3BH_3 catalyzed by $LiNbWO_6$ decorated with platinum nanoparticles (PtNPs) initially involves the adsorption of NH_3BH_3 on the surface of the PtNPs, while the water molecule is activated on the $LiNbWO_6$ support, generating reactive species that provide the protons essential for the reaction. The synergistic interaction between the support and the PtNPs allows the simultaneous transfer of hydrogens originating from NH_3BH_3 and water to the catalytic surface, where adsorbed atomic hydrogen is formed. The recombination of these hydrogen atoms results in the release of molecular H_2. Water acts as a limiting factor in the process, indicating that the availability of this reagent is crucial for reaction efficiency, as it directly participates in the generation step of the hydrogens that form hydrogen gas. Under light irradiation, the electronic excitation of $LiNbWO_6$ generates electron–hole pairs, where the holes, positively charged species with strong oxidizing power, promote the partial oxidation of adsorbed water, facilitating the breaking of the O–H bond and the generation of activated protons. These protons are transferred to the PtNPs, where recombination into molecular H_2 occurs. Experiments with hole inhibitors demonstrated that catalytic activity under light was similar to that observed in the dark, confirming that the photocatalytic effect is directly associated with the generation and participation of holes. A schematic illustration of the reaction mechanism is presented in Fig. 6.

The band gap of bare $LiNbWO_6$ was measured to be 3.2 eV, which is consistent with the value of 3.02 eV reported by Hu *et al.* (2015).[63] The PtNPs/$LiNbWO_6$ composite, however, exhibited a reduced band gap of 2.73 eV. The PtNPs employed had an average size of 2.8 nm, which is small enough to create strong electronic interactions with the semiconductor surface, generating intermediate energy states that facilitate photon absorption and enhance the separation of photogenerated electron–hole pairs. Considering this band gap reduction, photons with wavelengths shorter than ~450–430 nm (violet/blue and UV) can effectively excite the semiconductor. The superior performance observed under natural light compared to

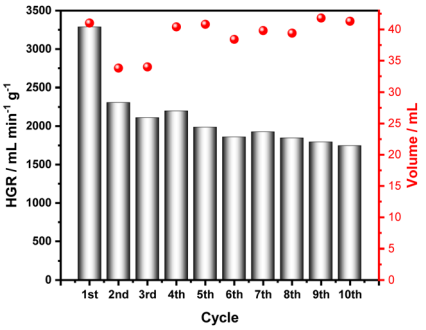

Fig. 7 Evaluation of different catalytic cycles in hydrogen evolution from NH_3BH_3 mediated by PtNPs/$LiNbWO_6$. Conditions: 20 mg of support, 3 mmol% of PtNPs, 0.58 mmol of NH_3BH_3, and temperature: 27 °C.

the UV lamp can be attributed to its broader spectral distribution and higher intensity in this wavelength range, promoting more efficient generation of electron–hole pairs and thus higher H_2 evolution.

The durability and performance of the system were evaluated and are shown in Fig. 7. A decrease in the hydrogen generation rate (HGR) was observed from the first to the second cycle, after which it remained stable over the following nine cycles. However, the reaction yield remained consistent throughout all ten cycles, indicating that hydrogen generation can be effectively reinitiated by the reinjection of AB for at least ten consecutive cycles. In Fig. S12 and S13, XPS analysis confirms that the catalyst remained stable after use, which explains the consistent performance over 10 consecutive cycles.

4. Conclusion

These results led us to conclude that $LiNbWO_6$ was successfully synthesized *via* a solvent-free solid-state method. This material proved to be an efficient support for platinum nanoparticles in the catalytic hydrolysis of ammonia borane for hydrogen generation, achieving a hydrogen generation rate (HGR) of 3974 mL H_2 $min^{-1} \cdot g^{-1}$, a value comparable to those reported in the literature. The stability of the catalyst was evaluated over 10 consecutive cycles, maintaining its catalytic efficiency, which confirms its robustness. These results indicate that $LiNbWO_6$ is a promising material for hydrogen generation applications as an energy source, contributing to the achievement of United Nations Sustainable Development Goal (SDG) No. 7 – Affordable and Clean Energy.

Author contributions

Noemí Cristina Silva de Souza: data curation, formal analysis, investigation, methodology, validation; writing – original draft; Beatriz Rodrigues Olímpio: data curation, formal analysis, investigation, methodology, validation; Gessica do Carmo Dias: formal analysis, investigation, methodology; Juliana Peña Gomes: formal analysis, investigation, methodology; Kleryton Luiz Alves de Oliveira: formal analysis; Didier Astruc: conceptualization, supervision and writing – review and editing; Tiago Almeida Silva: investigation, review and editing; Geraldo Magela de Lima: conceptualization, supervision, investigation, review and editing; Renata Pereira Lopes Moreira: conceptualization, funding acquisition, project administration, supervision, writing – review and editing.

Conflicts of interest

There are no conflicts to declare.

Data availability

The data supporting the conclusions of this study are available in the supplementary file (SI). Supplementary information is available. See DOI: https://doi.org/10.1039/d5ra04670j.

Acknowledgements

The authors express their gratitude to the Coordenação de Aperfeiçoamento de Pessoal de Nível Superior - Brazil (CAPES), the Conselho Nacional de Desenvolvimento Científico e Tecnológico (CNPq, 312400/2021-7, 405828/2022-5, 305649/2021-3, and 407799/2022-2), and the Fundação de Amparo à Pesquisa do Estado de Minas Gerais (FAPEMIG, RED-00144-22, APQ-01275-18, and APQ-03572-23), the University of Bordeaux and the Centre National de la Recherche Scientifique (CNRS) for their financial support. The authors also thank the Departments of Chemistry and Physics at the Universidade Federal de Viçosa for providing access to equipment and technical assistance. During the development of this proposal, ChatGPT was used exclusively for grammatical review. All ideas and technical content are the sole responsibility of the authors.

References

1 J. Chen, B. Long, H. Hu, Z. Zhong, I. Lawa, F. Zhang, L. Wang and Z. Yuan, *Int. J. Hydrogen Energy*, 2022, **47**, 2976–2991.
2 Y. Chen, Z. Lang, K. Feng, K. Wang, Y. Li, Z. Kang, L. Guo, J. Zhong and J. Lu, *Nat. Commun.*, 2024, **15**, 9113.
3 S. Ghosh, S. R. Kadam, L. Houben, R. Bar-Ziv and M. Bar-Sadan, *Appl. Mater. Today*, 2020, **20**, 100693.
4 H. He, L. Zeng, X. Peng, Z. Liu, D. Wang, B. Yang, Z. Li, L. Lei, S. Wang and Y. Hou, *Chem. Eng. J.*, 2023, **451**, 138628.
5 M. Amin, H. H. Shah, A. G. Fareed, W. U. Khan, E. Chung, A. Zia, Z. U. Rahman Farooqi and C. Lee, *Int. J. Hydrogen Energy*, 2022, **47**, 33112–33134.
6 M. G. Rasul, M. A. Hazrat, M. A. Sattar, M. I. Jahirul and M. J. Shearer, *Energy Convers. Manage.*, 2022, **272**, 116326.
7 B. Azizimehr, T. Armaghani, R. Ghasemiasl, A. Kaabi Nejadian and M. A. Javadi, *Int. J. Hydrogen Energy*, 2024, **72**, 716–729.
8 M. Liu, Z. Yao, J. Gu, C. Li, X. Huang, L. Zhang, Z. Huang and M. Fan, *Chem. Eng. J.*, 2023, **461**, 141918.
9 H. He, J. Xiao, Z. Liu, B. Yang, D. Wang, X. Peng, L. Zeng, Z. Li, L. Lei, M. Qiu and Y. Hou, *Chem. Eng. J.*, 2023, **453**, 139751.

10 P. D. Sanadi, R. K. Chougale, D. B. Malavekar, J. H. Kim, S. Masimukku, G.-P. Chang-Chien, Y.-C. Ling, S. S. Kolekar and G. S. Kamble, *Sci. Rep.*, 2025, **15**, 16074.
11 A. Kazemi, F. Manteghi and Z. Tehrani, *ACS Omega*, 2024, **9**, 7310–7335.
12 G. H. Sperandio, J. P. de Carvalho, C. B. R. de Jesus, I. M. Junior, K. L. A. de Oliveira, G. A. Puiatti, J. R. de Jesus and R. P. L. Moreira, *Int. J. Hydrogen Energy*, 2024, **83**, 774–783.
13 M. Navlani-García, K. Mori, Y. Kuwahara and H. Yamashita, *NPG Asia Mater.*, 2018, **10**, 277–292.
14 C. Milanese, T. R. Jensen, B. C. Hauback, C. Pistidda, M. Dornheim, H. Yang, L. Lombardo, A. Zuettel, Y. Filinchuk, P. Ngene, P. E. de Jongh, C. E. Buckley, E. M. Dematteis and M. Baricco, *Int. J. Hydrogen Energy*, 2019, **44**, 7860–7874.
15 T. Wang, J.-R. Hamon, C. Wang and D. Astruc, *Coord. Chem. Rev.*, 2025, **544**, 216871.
16 O. V. Komova, V. I. Simagina, V. R. Butenko, G. V. Odegova, O. A. Bulavchenko, O. A. Nikolaeva, A. M. Ozerova, I. L. Lipatnikova, E. S. Tayban, S. A. Mukha and O. V. Netskina, *Renew. Energy*, 2022, **184**, 460–472.
17 J. Huo, K. Zhang, H. Wei, L. Fu, C. Zhao, C. He and X. Hu, *Chin. Chem. Lett.*, 2023, **34**, 108280.
18 S. Garrido Nuñez, D. L. Schott and J. T. Padding, *Int. J. Hydrogen Energy*, 2025, **97**, 640–648.
19 D. Geniş, B. Coşkuner Filiz, S. Kılıç Depren and A. Kantürk Figen, *Microporous Mesoporous Mater.*, 2020, **305**, 110363.
20 N. Tunç and M. Rakap, *Catal. Sci. Technol.*, 2020, **10**, 7865–7874.
21 L. Semiz, *Chem. Phys. Lett.*, 2021, **767**, 138365.
22 Y. Pei, Y. Niu, W. Zhang, Y. Zhang, J. Ma and Z. Li, *Int. J. Hydrogen Energy*, 2022, **47**, 2819–2831.
23 S. Akbayrak and S. Özkar, *Int. J. Hydrogen Energy*, 2018, **43**, 18592–18606.
24 G. M. Bousada, V. Nogueira da Silva, B. Fernandes de Souza, R. S. de Oliveira, I. Machado Junior, C. H. F. da Cunha, D. Astruc, R. R. Teixeira and R. P. Lopes Moreira, *RSC Adv.*, 2024, **14**, 19459–19471.
25 B. Gong, H. Wu, L. Sheng, W. Zhang and X. Wu, *ACS Appl. Mater. Interfaces*, 2022, **14**, 13231–13239.
26 W. Xu, W. Li, H. Wen, J. Ding, Y. Liu, W. Li and B. Li, *Appl. Catal., B*, 2021, **286**, 119946.
27 L. Oliveira, M. Pereira, A. Pacheli Heitman, J. Filho, C. Oliveira and M. Ziolek, *Molecules*, 2023, **28**, 1527.
28 X. Cheng, T. Liu, H. Yu, F. Ran, W. Ye, H. Zhu, M. Shui, Y. Xie and J. Shu, *Chem. Mater.*, 2020, **32**, 3376–3384.
29 Z. Fan, L. Sun, S. Wu, C. Liu, M. Wang, J. Xu, X. Zhang and Z. Tong, *J. Mater. Sci.*, 2019, **54**, 10204–10216.
30 Z. Ali, I. Khan, M. Rahman, R. Ahmad and I. Ahmad, *Opt. Mater.*, 2016, **58**, 466–475.
31 S. Wu, C. Li, H. Wei, X. Song, L. Liu and J. Xu, *Mater. Today Commun.*, 2022, **33**, 104492.
32 J. He, Q. J. Li, Y. Tang, P. Yang, A. Li, R. Li and H. Z. Li, *Appl. Catal., A*, 2012, **443–444**, 145–152.
33 A. A. Levchenko, G. Li, J. Boerio-Goates, B. F. Woodfield and A. Navrotsky, *Chem. Mater.*, 2006, **18**, 6324–6332.
34 W. Chen, Z. Wang, X. Duan, G. Qian, D. Chen and X. Zhou, *Chem. Eng. Sci.*, 2018, **192**, 1242–1251.
35 M. Asim, S. Zhang, B. Maryam, J. Xiao, C. Shi, L. Pan and J.-J. Zou, *Appl. Surf. Sci.*, 2023, **620**, 156787.
36 G. Fayad, P. Boullay and G. Clet, *J. Colloid Interface Sci.*, 2020, **570**, 41–51.
37 H. Bekkali and G. Clet, *Catal. Today*, 2025, **445**, 115076.
38 N. Kumari, K. Gaurav, S. K. Samdarshi, A. S. Bhattacharyya, S. Paul, B. Rajbongshi and K. Mohanty, *Sol. Energy Mater. Sol. Cells*, 2020, **208**, 110408.
39 K. Cordero-Edwards, L. Rodríguez, A. Calò, M. J. Esplandiu, V. Pérez-Dieste, C. Escudero, N. Domingo and A. Verdaguer, *J. Phys. Chem. C*, 2016, **120**, 24048–24055.
40 M. Thommes, K. Kaneko, A. V. Neimark, J. P. Olivier, F. Rodriguez-Reinoso, J. Rouquerol and K. S. W. Sing, *Pure Appl. Chem.*, 2015, **87**, 1051–1069.
41 N. Wang, M.-Y. Zhao, Z.-W. Yin and W. Li, *Mater. Lett.*, 2003, **57**, 4009–4013.
42 H. Zhai, H. Liu, H. Li, L. Zheng, C. Hu, Z. Wang, J. Qi and J. Yang, *Nanoscale Res. Lett.*, 2017, **12**, 496.
43 A. Uzundurukan and Y. Devrim, *Int. J. Hydrogen Energy*, 2019, **44**, 26773–26782.
44 Z. Jichao, W. Yuan, H. Jie, H. Lifang and D. RuiJ, *Phys. Chem. Solids*, 2019, **126**, 33–42.
45 J. Wang, S. Rathi, B. Singh, I. Lee, H. I. Joh and G. H. Kim, *ACS Appl. Mater. Interfaces*, 2015, **7**, 13768–13775.
46 S. Özkar, *Dalton Trans.*, 2021, **50**, 12349–12364.
47 S. Guan, Z. Yuan, S. Zhao, Z. Zhuang, H. Zhang, R. Shen, Y. Fan, B. Li, D. Wang and B. Liu, *Angew. Chem., Int. Ed.*, 2024, **63**, e202408193.
48 C. Wang, J. Tuninetti, Z. Wang, C. Zhang, R. Ciganda, L. Salmon, S. Moya, J. Ruiz and D. Astruc, *J. Am. Chem. Soc.*, 2017, **139**, 11610–11615.
49 F. Fu, C. Wang, Q. Wang, A. M. Martinez-Villacorta, A. Escobar, H. Chong, X. Wang, S. Moya, L. Salmon, E. Fouquet, J. Ruiz and D. Astruc, *J. Am. Chem. Soc.*, 2018, **140**, 10034–10042.
50 C. Wang, Q. Wang, F. Fu and D. Astruc, *Acc. Chem. Res.*, 2020, **53**, 2483–2493.
51 M. Sait Izgi, Ö. Şahin and C. Saka, *Mater. Manuf. Processes*, 2019, **34**, 1620–1626.
52 S. M. Mansur Ahmed, F. Salman, Y. Karataş, H. Ç. Kazıcı and M. Gülcan, *Int. J. Hydrogen Energy*, 2024, **90**, 369–385.
53 X. Qi, X. Li, B. Chen, H. Lu, L. Wang and G. He, *ACS Appl. Mater. Interfaces*, 2016, **8**, 1922–1928.
54 R. Xu, H. Li, L. Xu, Y. Pan, M. Ge, C. Wang and Z. Sun, *Chem. Eng. J.*, 2024, **479**, 147773.
55 C. Wang and D. Astruc, *Chem. Soc. Rev.*, 2021, **50**, 3437–3484.
56 J. Yang, F. Cheng, J. Liang and J. Chen, *Int. J. Hydrogen Energy*, 2011, **36**, 1411–1417.
57 A. Kantürk Figen and B. Coşkuner Filiz, *J. Colloid Interface Sci.*, 2019, **533**, 82–94.
58 C. Li, W. Meng, G. Hu, Y. Wang, Z. Cao and K. Zhang, *Int. J. Hydrogen Energy*, 2018, **43**, 17664–17672.
59 L. Li, B. Guo, H. Li, X. Zhang, Y. Feng and J. Liao, *Front. Mater.*, 2021, **8**, 638733.

60 S. Mehdi, Y. Liu, H. Wei, H. Zhang, R. Shen, S. Guan, X. Wu, T. Liu, H. Wen, Z. Peng, C. Wang, Z. Liu, H. Cao and B. Li, *Appl. Catal., B*, 2023, **325**, 122317.
61 J. Yang, Q. Yuan, Y. Liu, X. Huang, Y. Qiao, J. Lu and C. Song, *Inorg. Chem. Front.*, 2019, **6**, 1189–1194.
62 Y. Feng, F. Lv, H. Wang, X. Chen, H. Li, Z. Chen, G. Lin, J. Liao, M. He and Q. Liu, *Catal. Commun.*, 2021, **159**, 106343.
63 L.-F. Hu, R. Li, J. He, L. Da, W. Lv and J. Hu, *J. Nanophotonics*, 2015, **9**, 093041.